The Astrophysical Journal, 609:1018–1034, 2004 July 10
© 2004. The American Astronomical Society. All rights reserved. Printed in U.S.A.

THE HANLE EFFECT AS A DIAGNOSTIC OF MAGNETIC FIELDS IN STELLAR ENVELOPES. IV. APPLICATION TO POLARIZED P CYGNI WIND LINES

Richard Ignace,[1] Kenneth H. Nordsieck, and Joseph P. Cassinelli
Department of Astronomy, University of Wisconsin, 5534 Sterling Hall, 475 North Charter Street, Madison, WI 53706-1582
Received 2004 January 29; accepted 2004 March 23

ABSTRACT

The Hanle effect has been proposed as a new diagnostic of circumstellar magnetic fields for early-type stars, for which it is sensitive to field strengths in the 1–300 G range. In this paper we compute the polarized P Cygni line profiles that result from the Hanle effect. For modeling the polarization, we employ a variant of the "last scattering approximation." For cases in which the Sobolev optical depths are greater than unity, the emergent line intensity is assumed to be unpolarized, while for smaller optical depths, the Stokes source functions for the Hanle effect with optically thin line scattering are used. For a typical P Cygni line, the polarized emission forms in the outer wind, because the Sobolev optical depth is large at the inner wind. For low surface field strengths, weak P Cygni lines are needed to measure the circumstellar field. For high values of the surface fields, both the Zeeman and Hanle diagnostics can be used, with the Zeeman effect probing the photospheric magnetic fields and the Hanle effect measuring the magnetic field in the wind flow. Polarized line profiles are calculated for a self-consistent structure of the flow and the magnetic geometry based on the WCFields model, which is applicable to slowly rotating stellar winds with magnetic fields drawn out by the gas flow. For surface fields of a few hundred gauss, we find that the Hanle effect can produce line polarizations in the range of a few tenths of a percent up to about 2%.

Subject headings: polarization — stars: magnetic fields — stars: winds, outflows — techniques: polarimetric

1. INTRODUCTION

The Hanle effect is a diagnostic that refers to the modification of resonance line scattering polarization in the presence of a magnetic field. The effect begins to have an influence on the polarization at fairly small field strengths of just a few gauss, with sensitivity to fields up to around 300 G. Experiments to describe the polarization from resonance line scattering date primarily back to the first third of the 20th century (see Mitchell & Zemansky 1934). The influence of a magnetic field on line polarization was explained first by a young physicist named Wilhelm Hanle. Hanle (1924) described the change of linear polarization by the magnetic field in semiclassical terms as arising from the precession of an atomic, damped, harmonic oscillator. From a quantum mechanical point of view, the effect is understood in terms of interferences that occur when the degeneracy of the magnetic sublevels in the excited state is partially lifted. The effect has come to have applications to many topics in atomic physics, as described in Moruzzi & Strumia (1991).

Astrophysically, the Hanle effect has been used only in the Sun. Applications include magnetic field measurements in the chromosphere, corona, and particularly in prominences and filaments (e.g., see Lin et al. 1998). A detailed description of the physics of the Hanle effect and polarized radiation transport for solar studies appears in Stenflo (1994). However, in stellar astronomy, the Hanle effect remains relatively unutilized.

This paper is the fourth in a series that explores applications of the effect for other stars, especially hot stars with winds (Ignace et al. 1997, hereafter Paper I; Ignace et al. 1999, hereafter Paper II; Ignace 2001, hereafter Paper III). It has been our goal to develop model line profiles with the Hanle effect that can be used to interpret spectropolarimetric data for inferring the properties of circumstellar magnetic fields. The Zeeman effect has had some success in measuring *photospheric* surface fields for a few hot stars that are not part of the extreme Bp class (e.g., Henrichs 2003; Donati et al. 2001, 2002; Neiner 2002). However, Ignace & Gayley (2003) have shown that the Zeeman effect suffers serious technical challenges for use in diagnosing circumstellar magnetic fields from wind emission lines. For example, typical circular polarizations for such lines have peak values of only 0.01% for a field with a surface value of around 100 G. Fields of this magnitude can have a significant influence on the wind flow from hot stars (e.g., Maheswaran & Cassinelli 1992; Babel & Montmerle 1997a, 1997b; Cassinelli et al. 2002; ud-Doula & Owocki 2002). Small polarizations result for the Zeeman effect, because the Zeeman-split components that produce the circular polarization are incoherent and oppositely signed. The wavelength separation of the Zeeman split lines is small compared to typical astrophysical broadening effects. Consequently, the net circular polarization of the line is severely reduced, owing to polarimetric cancellation from blending of the Zeeman components. The Hanle effect is a *modification* of the linear polarization that arises from resonance line scattering that does not suffer from polarimetric cancellation due to line blending.

In a semiclassical description of the Hanle effect, the line scattering can be split into two parts: an isotropic scattering component and a dipole scattering component, such as free electrons (e.g., Hamilton 1947; Chandrasekhar 1960). The fraction of the scattering that is dipole-like is referred to as the "polarizability" E_1; the isotropic scattering contribution is given fractionally as $(1 - E_1)$. The introduction of a magnetic field induces a precession of the classical oscillator motion of the atomic scatterers. At the same time, the oscillations are damped, emitting their absorbed radiation at a rate given by the Einstein A-value for the transition of interest. Thus, there is a

[1] Currently at East Tennessee State University; ignace@etsu.edu.

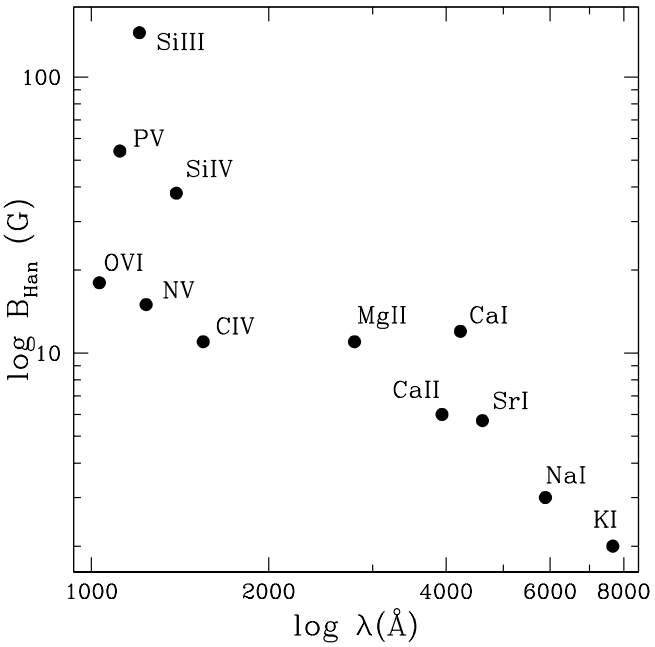

FIG. 1.—Plot of the Hanle field strength $B_{\rm Han}$ for resonance scattering lines common to astrophysics. Note that a few of these lines are singlets, but most are Li-like doublets. Of the doublets, only the shorter wavelength component will show a Hanle effect, since the longer wavelength component scatters isotropically and produces no line polarization. It is evident that shorter wavelength lines, having higher A-values, tend to have higher Hanle field values. The shorter wavelength lines are also associated with the more highly ionized atoms that are commonly observed in hot star winds.

competition between the radiative rate and the Larmor precessional rate, which has the frequency $\omega_{\rm L} = eB/m_e c$. Using these same arguments, Hanle (1924) deduced that a significant effect results when these two rates are somewhat comparable. We thus define the "Hanle ratio," given by

$$\frac{B}{B_{\rm Han}} = \frac{2g_{\rm L}\omega_{\rm L}}{A_{ul}} = g_{\rm L}\frac{B/5\ {\rm G}}{A_{ul}/10^8\ {\rm s}^{-1}}, \qquad (1)$$

where $g_{\rm L}$ is the Landé factor and A_{ul} is the Einstein A-value from upper level u to lower level l. The Hanle field strength $B_{\rm Han}$ is a conveniently defined parameter given by

$$B_{\rm Han} = \frac{m_e c A_{ul}}{2g_{\rm L}e}, \qquad (2)$$

which characterizes the magnetic field scale at which the Hanle effect is important. Values of $B_{\rm Han}$ for typical strong resonance lines common to astrophysics are displayed in Figure 1. Note that the lines at shorter wavelengths tend to have larger Hanle fields, because A-values increase roughly as λ^{-2}.

Recognizing that the Hanle effect is sensitive to modest field values of 10–100 G, we explored in Paper I its use for determining stellar wind magnetic field values and geometries from the total line polarization of optically thin emission lines. In Paper II we considered the Hanle effect in the optically thin and resolved line profiles that form in equatorial disks. In Paper III expressions were determined for the depolarizing effect of having stellar radiation arising from a finite disk instead of from a point star. For thin lines the correction was found to be the same as that for electron scattering polarization as derived by Cassinelli et al. (1987). It was pointed out by Cassinelli et al. (2001) that in contrast to the solar case, the application of the Hanle effect to hot stars is somewhat simpler and less ambiguous. This is for two reasons: (1) the hot star wind lines are far from LTE, so that virtually all bound electrons of metal species are in the ground state, whereas detailed non-LTE considerations are required in solar applications, and (2) the stellar continuum radiation that is being scattered is relatively "flat" over the frequency width of any given line, while solar applications often involve scattering of chromospheric emission lines for which the flux changes strongly with wavelength across the resonance line profiles.

The goal of these papers has been to move from an introduction of the Hanle effect for the broader stellar community to an investigation of its use by way of model calculations of increasing physical realism and numerical sophistication. In this paper we treat more realistic and more dynamically self-consistent magnetic field distributions in the wind, and we present results for the distribution of polarization across P Cygni line profiles.

Section 2 outlines the line polarization calculations and introduces a "single-scattering" approximation that is used together with traditional Sobolev line profile analyses. We find that line optical depth effects have a significant influence on the polarized line profiles. Heuristic results are described in § 3, including simple spherical shells with axial fields and spherical winds with dipole fields. Results for a more realistic scenario for the field and flow are presented in § 4. The model chosen for this is the slow magnetic rotator field configuration based on the WCFields theory by Ignace et al. (1998). Significant line polarizations of around 1% are found to result. Finally, § 5 offers a discussion of our modeling, with implications for observations of hot star winds at UV wavelengths and future directions for modeling efforts.

2. MODEL LINE PROFILES

In the previous papers we made calculations of the Hanle effect in emission lines that are valid only in the optically thin case. Here we extend the results to allow for optical depth effects, by implementing escape probability theory and introducing the single-scattering approximation for the emergent polarization from a volume sector. In this approximation the radiation at large optical depth is assumed to be completely unpolarized, and magnetically sensitive line polarization effects arise only in optically thin regions where a photon is considered to scatter only once. We make use of the Sobolev theory for resonance line scattering in stellar winds as developed by Sobolev (1960), Castor (1970), and Mihalas (1978). In Sobolev theory the radiative transfer is approximated as being local, because of the fast flow speeds and large velocity gradients that are present in stellar winds. The scattering and production of photons at any small volume in the medium can be assumed to have no interaction with any other portion of the flow.

2.1. *Standard Sobolev Theory*

In the standard Sobolev approach (e.g., as summarized in Mihalas 1978), the observable emission line profile is constructed from a ray-by-ray determination of the emergent line intensity for a fixed frequency within the line profile. An integration of these intensities is used to obtain the total emission or absorption at a particular frequency within the profile. The

key variables for computing the line emission for a spherical flow are the velocity shift along the line-of-sight axis z,

$$v_z = -v(r)\mu, \tag{3}$$

where v is the spherical velocity flow, r is the radial distance from the star, and $\mu = \cos\chi$ is the polar spherical angle from the observer's line of sight; the Sobolev optical depth

$$\tau_S = \frac{\kappa_l \rho \lambda_0}{(v/r)(1+\sigma\mu^2)}, \tag{4}$$

where κ_l is the frequency-integrated line opacity, $\rho = \rho(r)$ is the density, λ_0 is the line central wavelength, and σ is related to the line-of-sight velocity gradient (as given in eq. [13]); and the emergent intensity along the ray at impact parameter p,

$$I_\nu(p) = S_\nu(r)(1 - e^{-\tau_S}), \tag{5}$$

where $S_\nu(r)$ is the line source function.

Because the flow speed is much greater than the thermal broadening, only a small distance along the line of sight affects the intensity, and the integration over impact parameters at a fixed frequency in the line profile corresponds to an integral over an "isovelocity surface." Such a surface is defined by $v_z = \text{const}$. A simplification implicit in equation (5) is that the surfaces of constant velocity shift are single-valued with respect to intercepting rays of fixed p. More complicated cases involving nonlocal coupling associated with doublets or more general flow patterns are presented by Rybicki & Hummer (1978). Also common in applications of Sobolev theory is the distinct "core plus halo" approximation, in which there is a continuum-producing photosphere and a distinct overlying outflow and the absorption of the continuum is computed via $I_* e^{-\tau_S}$ along each ray intercepting the photosphere.

A different but equivalent approach based on escape probabilities was developed by Rybicki & Hummer (1983). The method involves integrating the emissivity for the line radiation over the emitting volume, accounting for optical depth effects via escape probabilities. This approach is more suitable for our purposes not because of nonlocal coupling or complicated flow patterns (for which we assume a radial velocity flow), but because we want to allow for axisymmetric magnetic field topologies viewed from arbitrary viewing inclinations. It is convenient to solve for the emergent polarized flux based on a volume integration over the scattering medium.

To describe our calculations, we begin with the basic escape probability approach to Sobolev theory. From Rybicki & Hummer (1983), the emergent luminosity from a volume element is

$$dL_\nu = 4\pi j_\nu \rho p_\mu r^2 \, dr \, d\alpha \, d\mu, \tag{6}$$

where $j_\nu \rho$ is the emissivity, given by

$$j_\nu \rho = \kappa_l \rho S_\nu \psi(\nu - \nu_z) \tag{7}$$

and p_μ is the directional escape probability, given by

$$p_\mu = \frac{1 - e^{-\tau_S}}{\tau_S} \tag{8}$$

for $\tau_S = \tau_S(r, \mu)$, the Sobolev optical depth as given previously. In equation (7) the factor ψ is the line profile function. In Sobolev theory this function is traditionally a delta function; however, it is only necessary that this function be much more narrow than the wind broadening of the line. For the fast winds of hot stars, this turns out to be an excellent approximation, since in the comoving frame of the gas, ψ has a velocity width of order $v_{\rm th}$ for a given ion species, and this is much smaller than the wind broadening, which is of order v_∞. The frequency ν_z appearing in the argument of ψ is related to the velocity shift of equation (3) by

$$\nu_z = \nu_0\left(1 - \frac{v_z}{c}\right), \tag{9}$$

for ν_0 the central wavelength of the line under consideration. The narrow profile response function ψ effectively picks out, for a given sight line, a particular volume element or "cell" corresponding to that cell's Doppler shift with $\nu = \nu_z$. Hence, the strong velocity gradients in hot star winds ensure that the radiative transfer for all volume elements is "local," meaning that all the cells are radiatively decoupled from each other.

The profile function ψ is defined such that

$$\int_0^\infty \psi(\nu - \nu')\, d\nu = 1. \tag{10}$$

For the purposes of numerical calculation, we consider a wind emission line profile to have a number of fixed frequency bins, each of width $\Delta\nu_z = (\nu_0/c)\Delta v_z = \Delta v_z/\lambda_0$ and in total spanning the full line width $\Delta\nu_\infty = (2v_\infty/c)\nu_0$. Then, for a given volumetric cell existing in a spherical shell at fixed radius r with fixed radial extent Δr, the luminosity contribution to the observed line emission is

$$\Delta L_\nu = 4\pi\kappa_l \rho S_\nu p_\mu r^2 \Delta r \Delta\alpha \frac{\Delta\mu}{\Delta\nu_z}. \tag{11}$$

Using the expression for the escape probability equation (8), the Sobolev optical depth equation (4), and the relation between $\Delta\nu_z$ and Δv_z, the luminosity from this cell becomes

$$\Delta L_\nu = 4\pi S_\nu (1 - e^{-\tau_S})\left(1 + \sigma\mu^2\right) v(r) r \Delta r \Delta\alpha \frac{\Delta\mu}{\Delta v_z}, \tag{12}$$

where

$$\sigma = \frac{d\ln v}{d\ln r} - 1. \tag{13}$$

It is the form of the Sobolev approximation given in equation (12) that we use for computing emission line profiles. In particular, pure scattering resonance lines are assumed, for which the source function is

$$S_\nu = \frac{\beta_c}{\beta_{\rm esc}} I_*, \tag{14}$$

where β represents the escape probability averaged over the relevant solid angle:

$$\beta(\mu) = \frac{1}{4\pi}\int_\Omega p_\mu \, d\Omega = \frac{1}{2}\int_\mu^{+1} p_\mu \, d\mu. \tag{15}$$

In particular, the two β's that occur in equation (14) are the penetration factor

$$\beta_c = \frac{1}{2}\int_{\mu_c}^{+1} p_\mu \, d\mu, \tag{16}$$

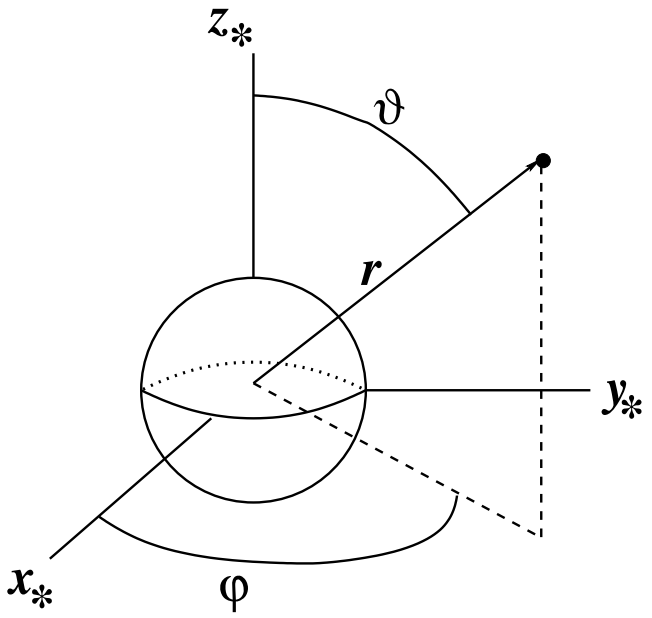

FIG. 2.—Stellar coordinate system, both Cartesian and spherical. The z_*-axis is taken as the reference direction for the field geometry. If the direction $\hat{\boldsymbol{r}}$ corresponds to the illumination ray of a scattering point at the filled circle, then $\vartheta = \vartheta_i$ and $\varphi = \varphi_i$.

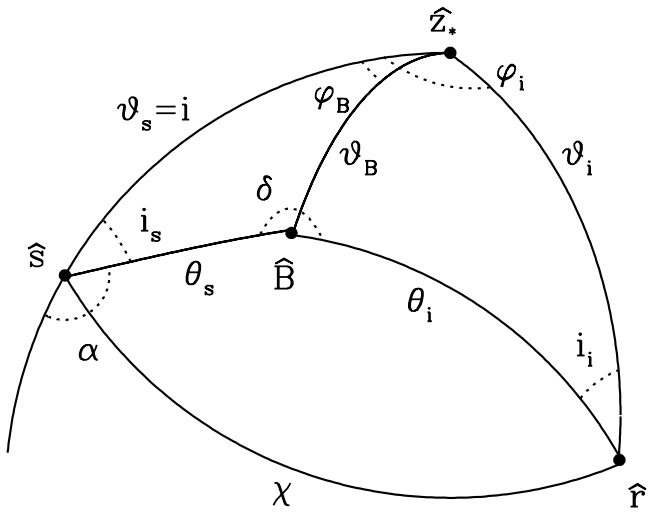

FIG. 3.—Scattering geometry centered at the scattering point of Fig. 2. The unit vectors $\hat{\boldsymbol{r}}$ and $\hat{\boldsymbol{s}}$ are for the radial direction and the scattering direction. The angles (χ, α) are polar spherical angles for the observer (along $\hat{\boldsymbol{s}}$). The angles ϑ_B and φ_B specify the vector orientation of the local magnetic field, B. The angles (θ, ϕ) are polar spherical angles for a system defined by this local magnetic field. The angle i_s is a Mueller rotation angle that rotates the Q- and U-polarizations from the reference frame of the magnetic field to that of the observer's measurement axes.

for $\mu_c = (1 - R_*^2/r^2)^{1/2}$, and the escape factor

$$\beta_{\rm esc} = \frac{1}{2}\int_{-1}^{+1} p_\mu \, d\mu. \tag{17}$$

It is useful to compare the thin and thick limits for the source function. For regions where $\tau_{\rm S} \ll 1$ for all μ, one has from equation (8) that $p_\mu \approx 1 - O(\tau_{\rm S})$. In this case $\beta_c \approx 0.5(1 - \mu_c)$ and $\beta_{\rm esc} \approx 1$. Thus, the ratio of β's yields the well-known dilution factor

$$W(r) = \frac{1}{2}\left(1 - \sqrt{1 - \frac{R_*^2}{r^2}}\right). \tag{18}$$

The thick limit with $\tau_{\rm S} \gg 1$ is quite different. The escape probability becomes $p_\mu \approx \tau_{\rm S}^{-1} = f(r)[1 + \sigma(r)\mu^2]$, for $f(r)$ a function of radius only. For a spherical shell of radius r, this escape probability factor is a parabola in μ, and thus a parabola also in Doppler shift in contributing to the line profile emission. For typical wind velocity laws that increase monotonically from some small value to an asymptotically large value, σ ranges from $\sigma \approx -1$ to $\sigma \gg 1$. This implies that the parabolic factor can be either concave up or concave down, and this behavior affects the line profile. The exact form of the source function thus depends on the velocity law $v(r)$, and for our model line profile calculations, a typical beta wind velocity law (which to avoid confusion with the escape probabilities is written using γ) is adopted, as given by

$$v(r) = v_\infty\left(1 - \frac{bR_*}{r}\right)^\gamma, \tag{19}$$

where γ is the velocity law exponent and $b < 1$ sets the initial wind speed v_0. For such a form, and with $\gamma = 1$, it can be shown that in the optically thick limit, the source function varies as $S_\nu \propto r^{-3}$.

Having described the source functions for wind emission lines in the standard Sobolev approach, we turn now to a discussion of the polarizing properties of the Hanle effect.

2.2. *The Hanle Source Functions for Single Scattering*

Computing the polarimetric properties of a beam of line radiation that is modified by the Hanle effect requires a number of coordinate transformations involving the local magnetic field at the scattering point, the star-centered frame, and the observer's coordinate frame. Figure 2 shows both the Cartesian (x_*, y_*, z_*) and spherical (r, ϑ, φ) stellar coordinates. The filled circle in Figure 2 represents a point of scattering, with the scattering geometry shown in Figure 3. There, the unit vector $\hat{\boldsymbol{s}}$ for the scattered light is in the direction toward the observer (i.e., along the z-axis). The spherical angle χ is the angle of scattering from the radial direction, and α is the angle to the local field direction. Cylindrical coordinates (p, α, z) refer to the observer, with p being the impact parameter (not shown in the figure). We take the star to be axisymmetric and tilted with respect to the observer's axis by an inclination angle i.

The field topology is also assumed to be axisymmetric about the axis z_* and star-centered. In the star system, the orientation of the vector magnetic field at any point in the wind is given by the polar angles ϑ_B and φ_B. Polar angles θ_s and θ_i refer to the direction, measured from the local magnetic field axis $\hat{\boldsymbol{B}}$, of the scattered light and the radial direction, respectively, where the local radius vector $\hat{\boldsymbol{r}}$ is taken to be the symmetry axis for the incident bundle of intensities from the stellar atmosphere. We ignore limb darkening so that stellar intensities I_* are the same from every point of the projected photosphere. Azimuthal angles ϕ_s and ϕ_i are measured around $\hat{\boldsymbol{B}}$. It is only their difference that enters into the phase function that governs the Hanle effect, so we define $\delta = \phi_s - \phi_i$, which is what appears in Figure 3. Details regarding the interrelations of the various geometric angles and their evaluation are given in Appendix A.

The Stokes parameters I, Q, U, and V are used to describe the polarization of the light, which is represented as a "vector"; for example, the flux of light is $\boldsymbol{F} = (F_I,\ F_Q,\ F_U,\ F_V) = \boldsymbol{L}/4\pi D^2$. However, we always assume that $V = 0$ (i.e., the circular polarization is zero), and so ignore that component in what follows.

For the Stokes source function, we have $\boldsymbol{S} = (S_I,\ S_Q,\ S_U)$. In Papers I–III, expressions were given for the source function elements, which are repeated here in modified form:

$$S_I = S_{II}, \tag{20}$$

$$S_Q = S_{QI}\cos 2i_s + S_{UI}\sin 2i_s, \tag{21}$$

$$S_U = -S_{QI}\sin 2i_s + S_{UI}\cos 2i_s, \tag{22}$$

where S_{II}, S_{QI}, and S_{UI} are the source functions in the magnetic field system and i_s is an azimuthal angle between that system and the observer's (see Fig. 2). The source function components are

$$\begin{aligned} S_{II} = J + \frac{3}{8}E_1(3K - J)\Bigg[&\frac{1}{6}\left(1 - 3\cos^2\theta_i\right)\left(1 - 3\cos^2\theta_s\right) \\ &+ a(B,\ \delta)\cos\theta_s\cos\theta_i\sin\theta_s\sin\theta_i \\ &+ \frac{1}{2}c(B,\ \delta)\cos^2\theta_i\sin^2\theta_s\Bigg], \end{aligned} \tag{23}$$

$$\begin{aligned} S_{QI} = \frac{3}{8}E_1(3K - J)\Bigg[&\frac{1}{2}\sin^2\theta_s\left(1 - 3\cos^2\theta_i\right) \\ &+ a(B,\ \delta)\cos\theta_s\cos\theta_i\sin\theta_s\sin\theta_i \\ &- \frac{1}{2}c(B,\ \delta)\sin^2\theta_i\left(1 - \cos^2\theta_s\right)\Bigg], \end{aligned} \tag{24}$$

$$\begin{aligned} S_{UI} = \frac{3}{8}E_1(3K - J)\Big[&- b(B,\ \delta)\cos\theta_i\sin\theta_i\sin\theta_s \\ &+ d(B,\ \delta)\cos\theta_s\sin^2\theta_i\Big], \end{aligned} \tag{25}$$

where E_1 is the polarizability, J and K are the standard Eddington moments of the radiation field (assumed to be determined by the incident stellar radiation field), and the local field strength enters through the functions a, b, c, and d, which are given by

$$a = \cos\alpha_1\cos(\delta - \alpha_1), \tag{26}$$

$$b = \cos\alpha_1\sin(\delta - \alpha_1), \tag{27}$$

$$c = \cos\alpha_2\cos 2(\delta - \alpha_2), \tag{28}$$

$$d = \cos\alpha_2\sin 2(\delta - \alpha_2), \tag{29}$$

where each α is defined by

$$\tan\alpha_m = m\frac{g_{\rm L}eB}{m_e c} = \frac{m}{2}\frac{B}{B_{\rm Han}}, \tag{30}$$

for $g_{\rm L}$ the Landé factor and $m = 1$ or 2. The case of nonmagnetic scattering corresponds to $\alpha_m = 0$, for which the scattering source functions reduce to the expressions for pure Thomson (dipole) scattering, except for E_1. In the strong or "saturated" limit of the Hanle effect, $\alpha_m \approx \pi/2$, and so $a = b = c = d = 0$.

Finally, it is worth noting the analytic expressions for J and K in the current approximations. Assuming a star of uniform brightness, the Eddington moments are given by

$$J = \frac{1}{4\pi}\int I_*\, d\Omega = W(r)I_*, \tag{31}$$

$$K = \frac{1}{4\pi}\int I_*\mu^2\, d\Omega = W(r)I_*\left(\frac{1 + \mu_c + \mu_c^2}{3}\right). \tag{32}$$

The factor $\frac{1}{2}(3K - J)$ is the familiar finite star depolarization factor of Cassinelli et al. (1987). From the preceding two expressions, this geometric factor is given by

$$\frac{1}{2}(3K - J) = W(r)I_*\frac{1}{2}\mu_c(1 + \mu_c). \tag{33}$$

At large radius the factor scales as r^{-2}, which is the point-source approximation. However, right at the photosphere, it drops to zero. This results because the symmetry of the radiation field over half the sky as seen by a scattering particle yields no net polarization of the scattered light. On the other hand, limb darkening prevents the factor from entirely vanishing at the photospheric level. Although we ignore limb darkening in our models, the effect is relevant for the use of the Hanle effect in studies of the Sun that probe scattering geometries around the solar photospheric level (e.g., see Stenflo 1994).

2.3. *The Single-Scattering Approximation for Polarized Emission Lines*

It is well known that multiple scattering of linearly polarized light generally leads to a depolarization. The polarized intensity from most media of astrophysical interest is small, and so one can approximate the radiative transfer as being predominantly unpolarized. The depolarization that arises from multiple scattering would suggest that an emergent intensity beam derives the bulk of its polarization from its last scattering event. In the last-scattering approximation, radiation propagates through a medium as a beam of unpolarized radiation until it emerges, with a sense of polarization appropriate for its last scattering interaction.

For the wind case, it is a single-scattering approximation that is the picture most relevant for our analysis. In Sobolev theory the radiation transport for the line emission is localized to relatively small volumes, sometimes referred to as "resonance zones." In the terminology of Monte Carlo radiative transfer, one can envision many photon "packets" of stellar light that penetrate into these zones, scatter several times, and emerge toward an observer. Owing to the probabilistic nature of the treatment of the scattering, the scattering history of each packet is different. Although each is characterized by a polarization, the polarization position angles on average are random, thus summing to small net polarizations. In contrast, photon packets typically scatter only once inside optically thin resonance zones. These all have a polarization, but more importantly, on average they all have the same polarization position angle, so as to sum constructively. Consequently, we employ the simplifying assumption that the scattered light from optically thick ($\tau_{\rm S} > 1$) resonance zones is completely unpolarized, whereas light emerging from optically thin regions ($\tau_{\rm S} < 1$) is treated as if single-scattered, for which we use the Hanle source functions as previously defined.

3. RESULTS FOR AXIAL AND DIPOLE MAGNETIC FIELDS

In this section we present polarized profile results for heuristic purposes, focusing on two simple magnetic geometries: an axial magnetic field and a dipole magnetic field. In each case the underlying wind is assumed to be spherical. This latter assumption is not dynamically consistent with the chosen field topologies, but we adopt the condition so as to isolate the influence of the Hanle effect for the polarization of wind emission line profiles.

The viewing perspective is described completely by the inclination angle i in the stellar frame. Since many of the strong resonance lines common to astrophysics are Li-like doublets, we use $E_1 = 0.5$ for our calculations, which is the value appropriate for the shorter wavelength component for many of these doublets (e.g., Chandrasekhar 1960).

The line strength is characterized with an optical depth scale given by

$$\tau_l = \frac{\kappa_l \rho_0 \lambda_0}{v_\infty / R}, \tag{34}$$

and so the Sobolev optical depth can be expressed as

$$\tau_S = \tau_l w^{-2} x^{-1} (1 + \mu^2 \sigma)^{-1}, \tag{35}$$

with $w = v/v_\infty$ the normalized radial velocity and $x = r/R_*$ the normalized radius. Some example P Cygni profiles as calculated with our numerical code are shown in Figure 4 for a range of optical depth scales τ_l and with a $\gamma = 1$ velocity law. All of our model profile calculations involve $\gamma = 1$, and the case of $\tau_l = 1$ is typically adopted. For simplicity, we further assume that the ionization of the wind is constant with radius. The ionization of different atomic species is generally a function of radius (e.g., Drew 1989); however, some ions can be dominant over a substantial range of radii. Moreover, although variations in ionization can change the level of polarized flux, the percent polarization of the profile is not altered when ionization varies with radius only. For this reason we concentrate on the constant ionization case to emphasize the influence of the Hanle effect on the polarized line emission.

The different magnetic wind models are parameterized in terms of the ratio of the surface field strength B_* relative to the Hanle field $B_{\rm Han}$. Since the figures display polarized line profiles for a range of ratios $B_*/B_{\rm Han}$, one can view the results in two different fashions. For a line with a given Hanle field, different polarized profiles represent how the line would appear for stars of different surface field strengths. Conversely, for a star of a given field strength, the different polarized profiles represent lines of different Hanle fields from the same wind (i.e., assuming that all the lines form over the same spatial region). It is useful to scrutinize the results that follow with both perspectives in mind.

3.1. *The Axial Magnetic Field Case*

For an axial magnetic field, there is a tremendous simplification of the Hanle effect problem in terms of geometry, because the magnetic field $\boldsymbol{B} = B_* \hat{\boldsymbol{z}}_*$ is everywhere parallel to the assumed axis of symmetry for the star, with $\vartheta_B = 0$, and the field strength is taken to be constant. This then is the easiest case to consider for the Hanle effect. In fact, the expressions describing the Stokes Q and U source functions for the light scattered by an optically thin and uniform ring of matter whose symmetry axis passes through the origin are analytic. For a spherically symmetric wind, such a ring represents the fundamental building block for constructing theoretical emission line profiles.

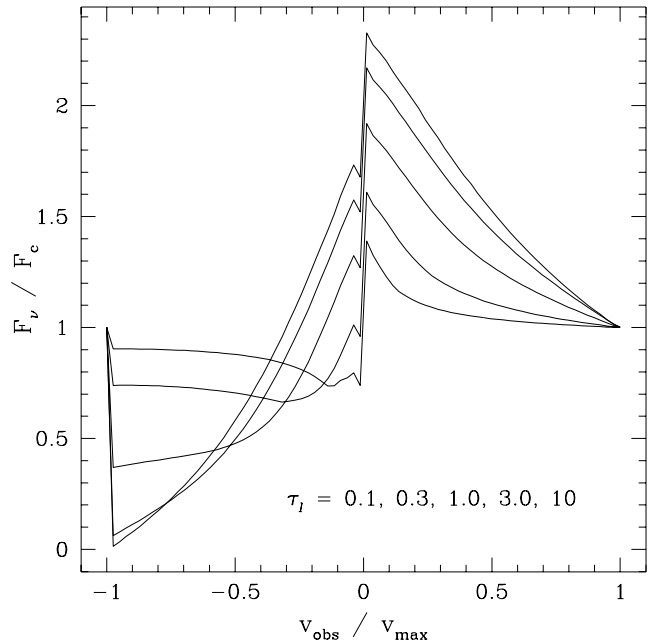

FIG. 4.—Sequence of P Cygni profiles produced by our code using the escape probability method with volume emissivity. The profiles are for optical depth scales τ_l as indicated, with thicker lines producing deeper blueshifted absorption and stronger redshifted emission. The dip that appears just blueward of line center in these profiles is real. In each case the wind velocity law is with $\gamma = 1$ and for an ion species of constant ionization fraction.

For the case at hand, spherical symmetry in the expansion and density, it is the scattered light as integrated around the ring that is important for our consideration of unresolved sources. Consider a ring whose axis is directed toward the observer. All points on the ring have the same Doppler shift. Note that the axis of the ring is not the same as the symmetry axis describing the magnetic field. Using equations (23)–(25) with $\theta_s = i$, $\theta_i = \vartheta$, $\delta = -\varphi$, and $i_s = 0$, the azimuthally integrated (i.e., in α) Stokes Q and U source functions for axisymmetric rings are found to be

$$S_Q = -\frac{3}{8} E_1 \sin^2 i \, S_0(r)\left(1 - 3\cos^2\chi\right)\Big[\left(1 - 3\cos^2 i\right) + 4\cos^2\alpha_1 \cos^2 i - \cos^2\alpha_2\left(1 + \cos^2 i\right)\Big], \tag{36}$$

$$S_U = \frac{3}{8} E_1 \cos i \sin^2 i \, S_0(r)\left(1 - 3\cos^2\chi\right) \times\left(-\sin 2\alpha_1 + \frac{1}{2}\sin 2\alpha_2\right), \tag{37}$$

where $S_0(r) = 3K - J$ is a function of radius only and the Hanle mixing angles α_1 and α_2 can vary with location $(r,\ \vartheta)$. Assuming for illustrative purposes that the field strength varies with radius only, several interesting points can be made about the Hanle effect in emission lines.

Consider an optically thin spherical scattering shell. Each isovelocity contour is a ring centered on the observer's viewing axis and distinguished from other rings by the angle χ. Figure 5 shows how the Q and U source functions vary from

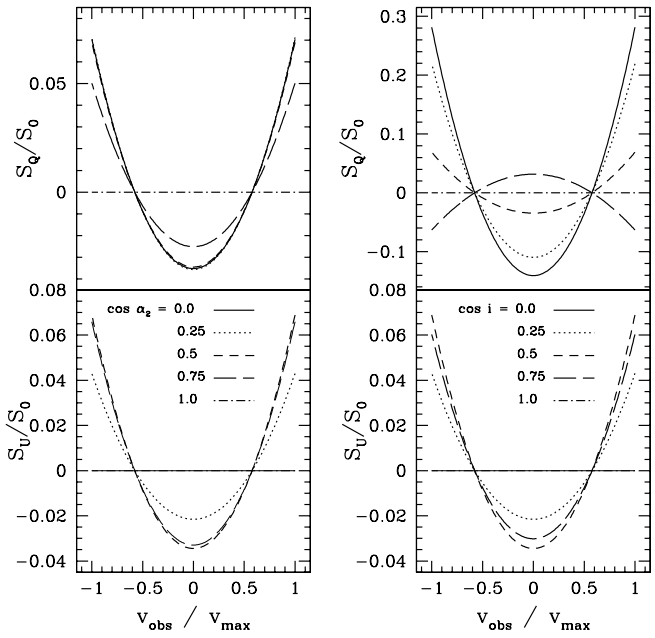

FIG. 5.—Variation of S_Q and S_U across an expanding and optically thin spherical shell that is threaded by an axial magnetic field of constant strength. The Stokes source functions are plotted against observed Doppler shift, from the front side at $v_{obs}/v_{max} = -1$ to the rear side at $v_{obs}/v_{max} = +1$. *Left panels*: For fixed $\cos i = 0.5$, the effect of varying the Hanle effect via the parameter $\cos\alpha_2 = 1.0$, 0.75, 0.5, 0.25, and 0.0 for $B/B_H = 0.0$, 0.9, 1.7, 3.9, and ∞. *Right panels*: For fixed $\cos\alpha_2 = 0.5$, the effect of varying the viewing inclination (with the solid line for $i = 90^\circ$ and the dot-dashed line for $i = 0^\circ$). Note that the top right panel uses a scale different from the other panels.

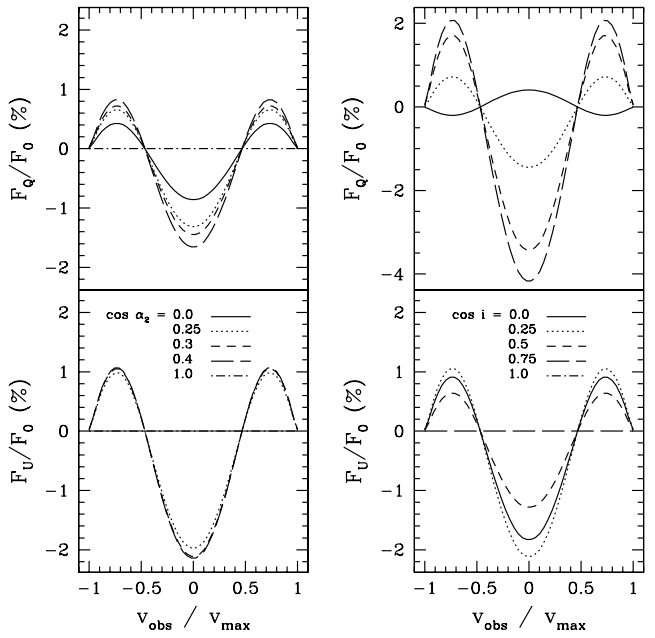

FIG. 6.—Results for the Q and U polarized flux profiles from our numerical code for an axial magnetic field of constant strength with $\tau_l = 1.0$ and $\gamma = 1$. The sequence of line types is the same as in Fig. 5, but the values used for $\cos\alpha_2$ have been changed slightly so that the profiles can more easily be seen. The left panels are for $\cos i = 0.5$ with different α_2 values, and the right panels are for $\cos\alpha_2 = 0.3$, but for different values of i. The vertical scale is different for the top right panel. The integrated polarized line flux in both Q and U is generally nonzero.

ring to ring, with a constant viewing inclination for the curves in the left panels and a constant field strength for the curves in the right panels.

Even though both the ring and field are axisymmetric, note that a U-signal persists. This is because of the field's handedness in producing the Hanle precession. Notable points include the following: (1) Both Q and U vanish for the case $B = 0$, since the nonmagnetic scattering polarization vanishes for a spherically symmetric density distribution. (2) The polarized Q and U source functions both vanish at the "Van Vleck" angle, $\cos^2\chi = \frac{1}{3}$. (3) The U-signal scales with inclination such that the U-polarization vanishes for pole-on and edge-on viewings. (4) For spherical expansion the U-profile integrates to zero across the line. (5) Finally, in the saturated limit of the Hanle effect, $S_U = 0$, and only a Q-signal remains. Indeed, in this limit the source function S_Q is especially simple, with the form

$$S_Q = -\frac{3}{8}E_1 \sin^2 i\, S_0(r)\left(1 - 3\cos^2\chi\right)\left(1 - 3\cos^2 i\right). \quad (38)$$

In addition to $S_Q = 0$ for the two isovelocity rings situated at $\cos^2\chi = \frac{1}{3}$, the Q source function also vanishes for viewing inclinations at $\cos^2 i = \frac{1}{3}$.

Figure 6 shows the polarized line profile (eq. [12]) for this geometry from our code, assuming a constant field strength and using the single-scattering approximation with $\gamma = 1$, $\tau_l = 1.0$, and $E_1 = 1$. Displayed are the continuum normalized Q and U Stokes flux profiles for an axial field and a spherical shell of fixed radius in percent polarization for the same range of viewing inclinations (relative to the axial field) as in Figure 5, but with a different selection of field strengths to better distinguish between the model line profiles. The vertical plot scale is different because the curves for Figure 5 are source functions, whereas those in Figure 6 are line fluxes. Since we explicitly assume that polarized line emission emerges only from optically thin portions of the wind, one might expect that the profiles that are evaluated numerically would resemble those of Figure 5, at least qualitatively. Indeed, the numerical polarized line profile and the analytic source function do show some similarity at line center, but whereas the analytic derivation predicts relatively strong polarization at the line wings, the polarized flux drops to zero for the numerical calculations. In particular, note that the line-integrated U-flux does not necessarily vanish, contrary to expectations.

These differences between the source function and line profile can be understood with the help of Figure 7, which shows an illustration with the star at center and dotted lines for isovelocity zones. The observer is along the z-axis located to the right. The solid curves are the loci of points with Sobolev optical depth $\tau_S = 1$ (assuming a velocity law with $\gamma = 1$ and line optical depth scales τ_l as indicated). For the given assumptions, interior to each set of paired solid curves, the line optical depth is greater than unity, and exterior the line optical depth is smaller than unity. The thick curves are for $\tau_l = 1$, which represents the case most typical of our line profile calculations. In this case the figure indicates that there is no spherical shell that can be drawn that does not intercept the region of $\tau_S > 1$. Moreover, the interception, for shells of large radius, occurs preferentially at those parts of the shell that are primarily fore and aft of the star with respect to the observer, thus corresponding to Doppler shifts in the line wings.

Importantly, we discover that there are two new effects that arise from a consideration of line optical depth effects. First, although spherical symmetry is used, the Sobolev optical depth for fixed radius varies in going from the front side of the shell to the rear side, with some portions being optically thick and others optically thin. Second, for some shells, every point can

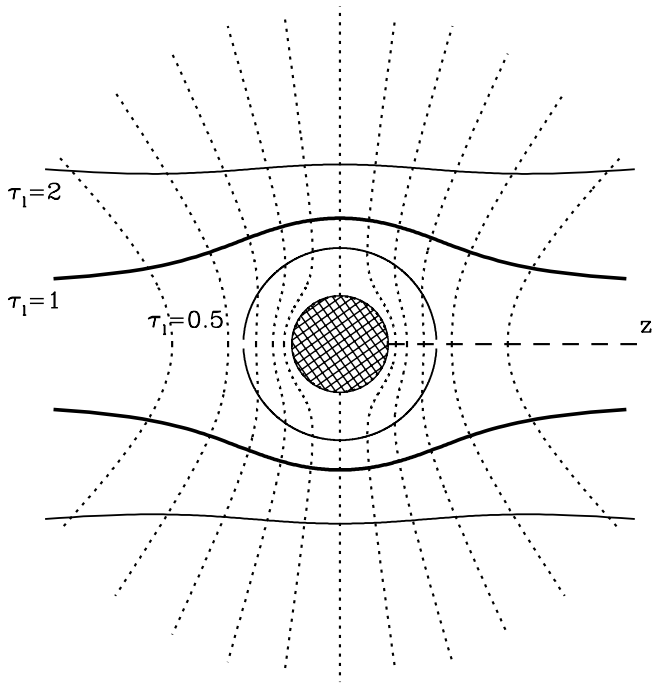

FIG. 7.—Isovelocity zones (*dotted lines*), with the observer to the right. The solid lines demarcate regions of the wind where the Sobolev optical depth in the line is thick ($\tau_S > 1$ interior to the curves) and thin ($\tau_S < 1$ exterior to the curves). Three cases are shown, with $\tau_l = 0.5$, 1, and 2. The $\tau_l = 1$ case is shown as a thick line, since it is the value adopted for most of our line calculations. In this particular case, some portion of every isovelocity zone is optically thick in the line. In the single-scattering approximation, polarized line emission is produced only at locations where $\tau_S < 1$.

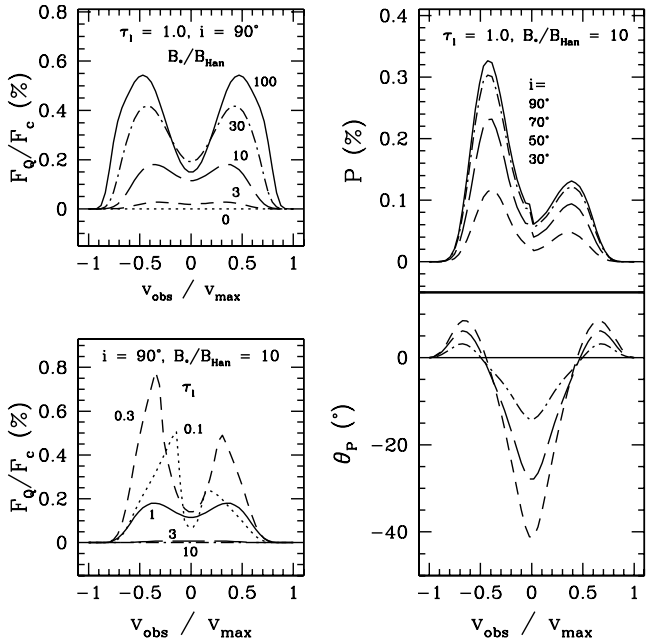

FIG. 8.—Percent polarization of the Hanle effect for a dipole magnetic field in a spherical stellar wind. *Top left*: Polarized Stokes Q-profiles as normalized to the continuum emission *outside* the line frequencies. For a dipole field as seen from the side in a line with $\tau_l = 1.0$, larger Hanle ratios (as labeled) yield higher line polarizations. *Bottom left*: As in the top left panel, except with τ_l varied as indicated for a fixed Hanle ratio. Note that the line asymmetry for the two lower optical depth cases is a consequence of stellar occultation. The strongest polarization results for fairly optically thin lines, which sample stronger fields deeper in the wind. *Top right*: Total polarization $P = (F_Q^2 + F_U^2)^{1/2}/F_{tot}$ in percent. The total flux F_{tot} includes the P Cygni line, which is inherently asymmetric in its profile shape. Overall, the effect of the viewing inclination is to reduce P for perspectives that are increasingly pole-on. *Bottom right*: Same line types as in the top right panel, but for the polarization position angle θ_P. Owing to symmetry, $U = 0$ at all points in the line for $i = 0°$ and 90°. A left-right symmetric U-profile remains for intermediate viewing inclinations (which spatially corresponds to fore-aft symmetry about the star).

be optically thick. For example, in the case $\tau_l = 1$, Figure 8 shows that every point inside $r \approx 2.5R_*$ has $\tau_S > 1$, and so the Hanle effect is effectively "blind" to the circumstellar magnetic fields between the wind base and this radius.

This latter point implies two interesting corollaries: First, lines of different strength (as characterized by the different τ_l values in the figure) allow the Hanle effect to probe magnetic fields to different radial proximities to the wind base. Second, the Hanle and Zeeman effects can be used in tandem. For a star such as θ^1 Ori C with a strong multikilogauss surface magnetic field, the Zeeman effect as applied to photospheric lines yields information about the surface field distribution and strength. The Hanle effect as applied to wind lines samples the circumstellar magnetic field, which is weaker than the surface field. Together, the line polarizations might be used to reconstruct how the magnetic field and wind flow affect one another.

In summary, considerations of the Hanle effect in a wind flow with an axial magnetic field reveal that substantial polarizations of up to 4% can result near line center. The Stokes Q- and U-profile shapes are characteristically symmetric, and the polarization position angle does not vary across the profile. A point that is significant for observational studies is that the line-integrated polarized flux does not in general vanish, implying that a net polarization could be measured even for poorly resolved line profiles. The axial field topology is especially simple, and the derived peak polarizations are to be considered as the *best possible*, because a constant vector magnetic field was assumed everywhere in the wind, whereas in real winds the field strength generally diminishes with radius and the field orientation normally varies from point to point. The major result of this section is that when using the axial field scenario as a control case, we find that line optical depth effects do substantially modify the shapes of the polarized profiles and the portions of the wind that can be probed by the Hanle effect.

3.2. *The Dipole Magnetic Field Case*

Now we apply our theory to extended and radially outflowing envelopes that are threaded with a dipole magnetic field. A dipole field and a radial wind are not compatible, since either a strong dipole field will result in wind confinement (Babel & Montmerle 1997a, 1997b; Cassinelli et al. 2002) or a strong wind flow will drag out the magnetic field, distorting the dipole into a more nearly radial geometry (ud-Doula & Owocki 2002). Still, the dipole case represents a more complicated field topology than offered by a simple axial field and so is worth investigating. In addition, this is the topology used in § 3.2 of Paper II, which had a more simplistic assumption for the effects of optical depth. Here we see the influence of optical depth in a better treatment of the radiative transfer.

It should be mentioned that a dipole magnetic field is purely radial at the poles, thus by symmetry yielding no Hanle effect. In the equatorial plane, the field is purely axial; everywhere else, the field is a vector sum of radial and latitudinal components. At no latitude is there a toroidal component of the

field. In § 4 the influence of a toroidal field is explored in the context of winds from slowly rotating stars.

Polarized line profiles have been calculated for a range of line strengths, viewing inclinations, and Hanle ratios, with the results displayed in Figure 8. The two left panels are for edge-on views with $i = 90°$. In this case Stokes U is identically zero throughout the line profile owing to symmetry, and so only Stokes Q is shown (normalized to the continuum flux F_c and plotted in percent). The profile polarization P and the variation of the polarization position angle θ_P are shown in the right panels. The Hanle ratios quoted in the figure refer to $B_*/B_{\rm Han}$; however, we recall that the field strength of a dipole diminishes with radius as $B \propto r^{-3}$, and so a range of radii and field strengths contribute to the observed line polarization.

Returning to the left panels, the top one shows that stronger Hanle ratios lead to lines of higher polarization. The left-right symmetry in the polarized profile corresponds to a fore-aft spatial symmetry with respect to the star. The panel below illustrates the effect of line optical depth, with the solid line for $\tau_l = 0.1$, short-dashed line for $\tau_l = 0.3$, long-dashed line for $\tau_l = 1$, dash-dotted line for $\tau_l = 3$, and dotted line for $\tau_l = 10$. For small optical depths, the polarized line emission arises from deep in the wind. As τ_l is made to increase, the region of $\tau_{\rm S} > 1$ moves outward, and the polarization peaks drift toward larger Doppler shifts in the line.

Initially, increasing τ_l leads to larger line polarizations, because there are more scatterers. For larger optical depths, the region of $\tau_{\rm S} > 1$ has swelled sufficiently in extent that the overall flux of polarized line emission begins to drop. Interestingly, at low values of τ_l, stellar occultation results in an asymmetric profile of polarized line flux, with the redshifted emission somewhat suppressed. For larger τ_l, the profile becomes symmetric. This can be understood in terms of Figure 7. For large τ_l, all the points lying directly behind and in front of the star do not contribute any polarized line emission, because those points all have $\tau_{\rm S} > 1$, and hence occultation has no influence; at small τ_l this is not case, and so occultation makes a difference.

Returning to Figure 8, the two right panels show the effects of viewing inclination, which in the case of a dipole field yields both Q- and U-profiles. The inclination values are indicated. The top plot is the total polarization with $P = (F_Q^2 + F_U^2)^{1/2}/F_{\rm tot}$, and the bottom plot is for the polarization position angle defined by $\tan 2\theta_P = F_U/F_Q$. Note that $F_{\rm tot}$ includes the redshifted P Cygni line emission and the blue-shifted absorption, making the polarized profile in P asymmetric. On the whole the line polarization is seen to drop with viewing inclination, similar to the $\sin^2 i$ rule of Brown & McLean (1977) for axisymmetric Thomson scattering envelopes.

The variation in the polarization position angle is especially interesting. Our assumption is that the polarization arises from the optically thin portions of the wind. This suggests that F_Q and F_U are roughly proportional in terms of optical depth effects. Therefore, the ratio F_U/F_Q that determines the polarization position angle θ_P is to first order independent of optical depth. Its amplitude is set by the viewing inclination, and its variation with Doppler shift is governed by the Hanle effect. The line types for θ_P in Figure 8 (*bottom right*) are the same as in the panel above it. In the absence of a magnetic field, the spherical symmetry ensures that both Q and U are zero, so that it is the Hanle effect that produces both the line polarization and the position angle variations. If the envelope and velocity field were instead axisymmetric, then position angle rotations could result even without a magnetic field. However, the Hanle effect would distinguish itself by virtue of how the position angle variations differed between lines of different A-values and optical depths.

In comparison to the polarized profiles from spherical winds that were modeled in Paper II (Fig. 8 in that work), the profile results presented here are seen to be qualitatively similar but to differ somewhat quantitatively. Under the single-scattering approximation, the polarized profiles have significant polarization near line center, whereas those of Paper II were more centrally depressed. Although the polarizations in Paper II were overestimated by about a factor of 2, the overall asymmetric profile shape in P remains because of the normalization by the P Cygni profile.

To sum up, the main lessons to draw from the dipole magnetic field case are that overall stronger line polarizations result from larger Hanle ratios, the strongest line polarizations are for lines that are relatively thin, the polarization is reduced for viewing inclinations that are farther from edge-on, and the influence of the Hanle effect is betrayed through the observation of position angle rotation effects in the line profile. Having established some insight into the Hanle effect of magnetized winds, and a general sense of the line polarizations that can result (up to about 0.7%), we next consider a more realistic case in the context of winds from slow rotators that drag out a relatively weak surface magnetic field.

4. RESULTS FOR A SLOW MAGNETIC ROTATOR

In this section, in order to define a realistic but tractable magnetic geometry, we assume that in the case of weak magnetic fields, the star will have a "slow magnetic rotator wind." This means that the field does not play a role in accelerating the flow to terminal velocity. We are motivated by the fact that the Sun is a slow magnetic rotator (Belcher & MacGregor 1976). The overall weak solar magnetic field does not dominate the wind flow but is believed to have contributed to a long-term braking of the Sun's rotation (as first analyzed by Weber & Davis 1967). The field produces some transfer of angular momentum to the wind, and in the process leads to some rotational distortion of the flow. For simplicity, we also assume that the rotation is slow enough that the wind velocity field is basically spherical and that the field is dragged out into "streak lines" by the flow. Although the velocity field is treated as a function of radius only, we consider both spherical and axisymmetric density distributions for the line polarization and the influence of the magnetic fields.

For the underlying field topology, we make use of the WCFields model (Ignace et al. 1998), which describes an initially radial field that is dragged out by the wind from a rotating star. The model is based on the wind-compression theory of Bjorkman & Cassinelli (1993). Expressions governing the wind flow and magnetic field geometry are summarized in Appendix B. The salient features are that (1) a given wind model is predominantly determined by the ratio of the equatorial rotation speed $v_{\rm rot}$ to the wind terminal speed v_∞, (2) the field is initially assumed to be radial at the wind base (i.e., a split monopole), (3) the fields are "weak" and frozen in so that the wind flow geometry determines the magnetic geometry, and (4) asymptotically, the field becomes dominantly toroidal at equatorial latitudes while remaining largely radial near the pole.

As described in Appendix B, we adopt approximate expressions to describe the flow and magnetic field that can be used for slowly rotating stars (i.e., $v_{\rm rot}/v_\infty \ll 1$). In this limit,

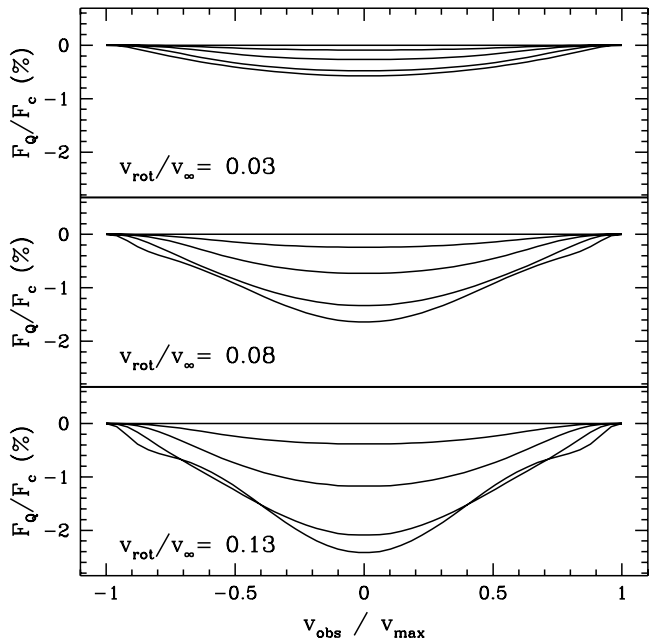

FIG. 9.—Polarized line profiles for slow magnetic rotators at three different values of $v_{\rm rot}/v_\infty$, as indicated. The magnetic geometries are determined by the WCFields model. The wind density and flow velocity are taken to be spherical, so that the polarization arises only from the Hanle effect itself. The different curves in each panel are for Hanle ratios of $B_*/B_{\rm Han} = 0$, 3, 10, 30, and 100, with stronger polarizations resulting for larger Hanle ratios. The inclination is 90°, and $\tau_l = 1$. A weak U-signal exists, but we choose not to show it here.

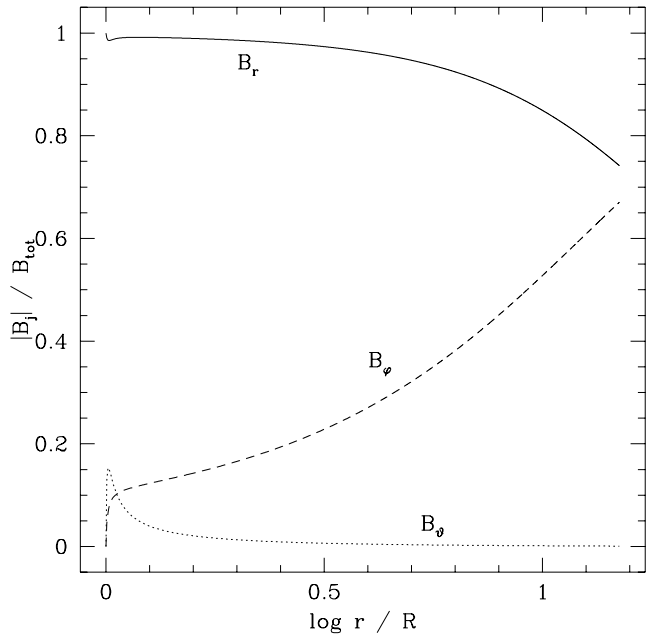

FIG. 10.—Variation of the magnetic field components from the WCFields model as a function of radius, using approximations that apply for slow stellar rotations. The individual components are normalized to the local total magnetic field strength. These curves are for the case $v_{\rm rot}/v_\infty = 0.08$ at a latitude of $\vartheta = 45°$ so as to roughly maximize the contribution of the latitudinal component B_ϑ.

spherical geometry for both the wind velocity and density can be adopted. As an example, a slow rotator model that can produce interesting line polarizations is the case $v_{\rm rot}/v_\infty = 0.08$. For a terminal speed of 2000 km s^{-1}, this would correspond to a rotation speed of 160 km s^{-1}, which is not atypical of observed $v \sin i$ values in O stars (e.g., Penny 1996) and amounts to rotating at about 25% of breakup. The asymptotic density contrast between the equator and pole, $\rho_{\rm eq}/\rho_{\rm pole}$, in this case is merely 1.25 (i.e., with $\gamma = 1$). Initially, we ignore this density variation in our models but return to the issue of how a wind density that deviates from spherical affects the line polarization.

4.1. *WCFields with a Spherical Wind Density*

Polarized flux profiles have been computed for the cases $v_{\rm rot}/v_\infty = 0.03$, 0.08, and 0.13, and the results are plotted as percent polarization in Figure 9. Only the Q-profiles are plotted. There is a U -profile, but the level of polarization is about an order of magnitude less than in Q, and so we do not show it. In each panel the different curves are for different Hanle ratios, with $B_*/B_{\rm Han} = 0$, 3, 10, 30, and 100, such that stronger polarizations result for larger Hanle ratios.

For all of these cases, the polarized profiles are seen to be single-peaked, in distinction from the dipole field case. The profiles also show a net negative polarization, implying a position angle that is orthogonal to the axis of rotation. This results from the significant toroidal magnetic field component and can be understood as follows: At the base of the wind, the field is initially a split monopole, with no toroidal component. Both toroidal and latitudinal components begin to develop as the flow draws the field out in radius (see Fig. 10, Appendix B). The radial component of the field decreases asymptotically as r^{-2}, whereas the toroidal component decreases as $r^{-1} \sin \vartheta$, and the latitudinal component as $r^{-3} \sin 2\vartheta$, for ϑ the stellar colatitude. At radii where the Sobolev optical depth is thin, the latitudinal field component is negligible (although it does account for the small level of U-polarization), and the toroidal component is starting to become comparable to B_r. The field is mainly radial near the poles, so that in these regions the Hanle effect is minor. Around the equator the field is becoming more and more toroidal.

Consider the isovelocity zone corresponding to line center, which is the plane of the sky as intercepting the center of the star. Without a magnetic field, the polarized intensity is symmetric about the line of sight to the star. By our convention the polarization is negative around the polar limb and positive around the equatorial limb. The field is radial near the pole, so the polarization of scattered line radiation does not change in that region. However, near the equator the toroidal field is into the plane on one side and out of it on the other. This leads to the geometry of the classic laboratory Hanle effect, and in the saturated limit the scattered light becomes completely depolarized. Integrating around a circle that is centered on the star and lies in this plane, it is clear that the net polarization is no longer zero but negative, being dominated by the unmodified polarized flux from the polar zones. Similar kinds of arguments can be used to show that the scattered light from all isovelocity zones will tend to be negative.

Figure 9 shows that the line polarization is stronger for more rapidly rotating stars. This just reflects the fact that in WCFields theory, $B_\varphi \sim v_{\rm rot}/v_\infty$, so that for a given location in the wind, faster rotation implies that the ratio B_φ/B_r at a given radius is larger. Figure 10 shows the variation of the field components with radius for a stellar colatitude of $\vartheta = 45°$, chosen such that the peak value of B_ϑ is roughly maximized. The field components are plotted as normalized to the total field strength $B_{\rm tot} = (B_r^2 + B_\vartheta^2 + B_\varphi^2)^{1/2}$. Since B_r dominates over most of the radii shown, the overall field strength drops

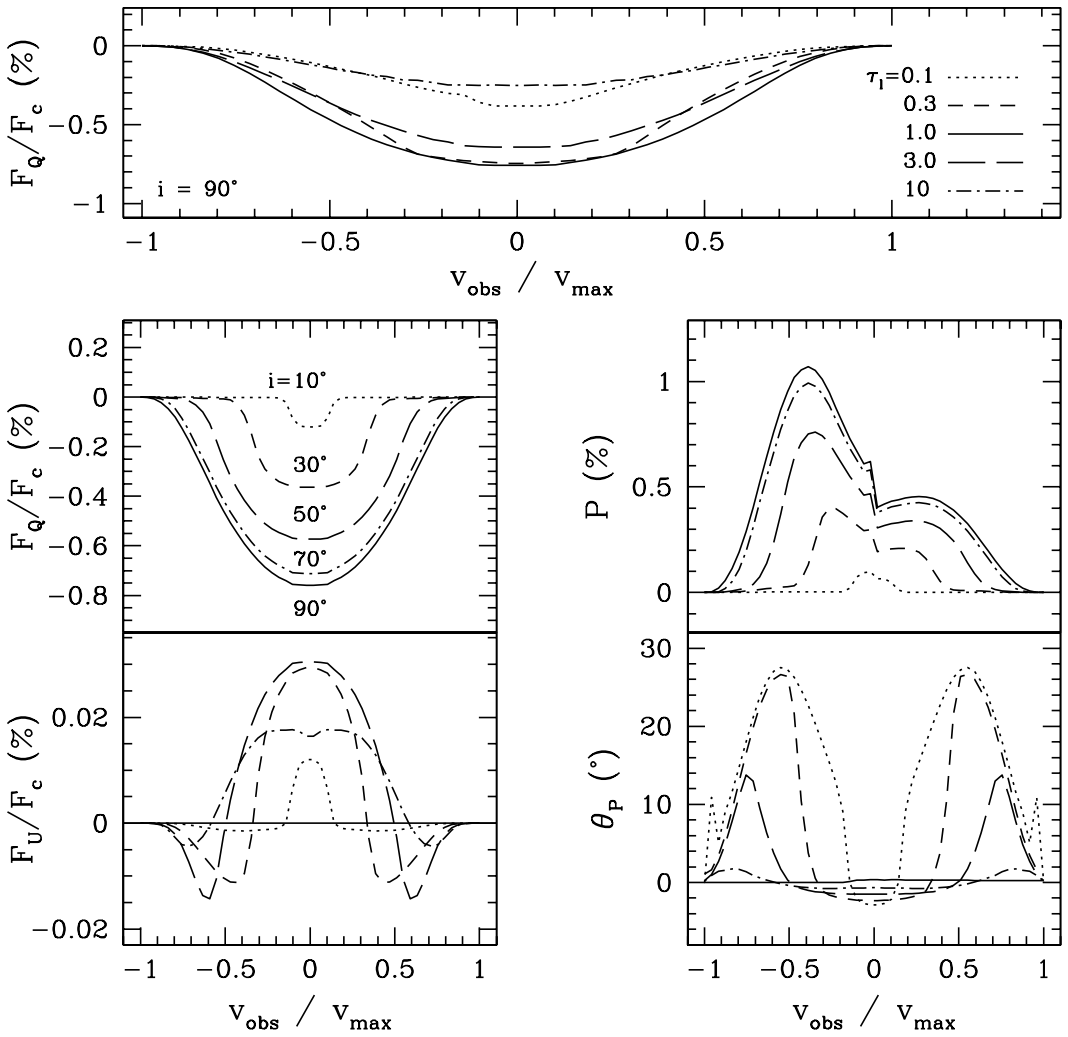

FIG. 11.—Series of polarized line profiles for a WCFields model with $v_{rot} = 0.08v_\infty$ to highlight the influence of optical depth and viewing inclination effects. The surface field strength is $B_* = 10B_{Han}$ for every profile. The top panel shows the continuum normalized Q-flux for $i = 90°$, with the line optical depth varied as indicated. The four panels below show the influence of viewing inclination for $\tau_l = 1.0$. *Left panels*: Plots of F_Q/F_c and F_U/F_c in percent polarization. *Right panels*: Plots of P (this being normalized to the full P Cygni line profile and not just the continuum level) and θ_P. The different curves are for the inclination values shown in the panel for F_Q.

roughly as r^{-2}, although somewhat less rapidly at the larger radii owing to the increasing importance of B_φ. As noted previously, at very large radius where the toroidal component dominates, the field decreases only inversely with radius, instead of quadratically. This figure is for the case of $v_{rot}/v_\infty = 0.08$; for faster rotations both the latitudinal and toroidal components would be relatively larger, and vice versa.

Especially important to realize is that the Hanle effect is nonlinear. Although the bulk of the scattered light that produces the polarized line flux comes from radii where τ_S is of order unity and somewhat less, Figure 10 indicates that the field is predominantly radial at these locations, which should yield no Hanle effect. Thus, it is the nonradial components that lead to a Hanle effect in terms of introducing an *asymmetry*, and yet the modification of the scattering polarization is determined by the *total* field strength, and so the radial field is still relevant. Consequently, the Hanle effect is in principle sensitive to the full three-dimensional magnetic field, in terms of field strength and field geometry. The main diagnostic challenge is the fact that the net line polarization at any frequency in the profile is a strongly convoluted property. At the very least, it is evident that larger Hanle ratios lead to greater polarization. Next we discuss observational prospects and diagnostic approaches.

Using the case of $v_{rot} = 0.08v_\infty$, we have examined the influence of line optical depth and viewing inclination in greater detail. Figure 11 shows a series of model line profiles at this fixed rotation speed as τ_l and i are varied. Figure 11 (*top*) shows the effect of line optical depth for the case $i = 90°$. Interestingly, line optical depth had a stronger influence on the line polarization in the dipole field case. Recall that as τ_l is made to increase, the region over which the line is optically thick grows in extent, and this region does not contribute to the line polarization. The field strength of a dipole decreases as r^{-3}, such that for $\tau_l \gtrsim 1$, the Hanle effect samples the magnetic field where even at modest radii it is quite small, so that the polarization is also small. The WCFields case is different. The field strength drops initially as r^{-2} for a split monopole, slowly transitioning to a predominantly toroidal field that decreases only as r^{-1}. This is much more gradual than for a dipole field, so that the line polarization does not drop significantly until τ_l becomes exceedingly thick: $\tau_l \gtrsim 3$. Indeed, the line polarization is larger for a somewhat thick line at $\tau_l = 10$ than for a thin line at $\tau_l = 0.3$,

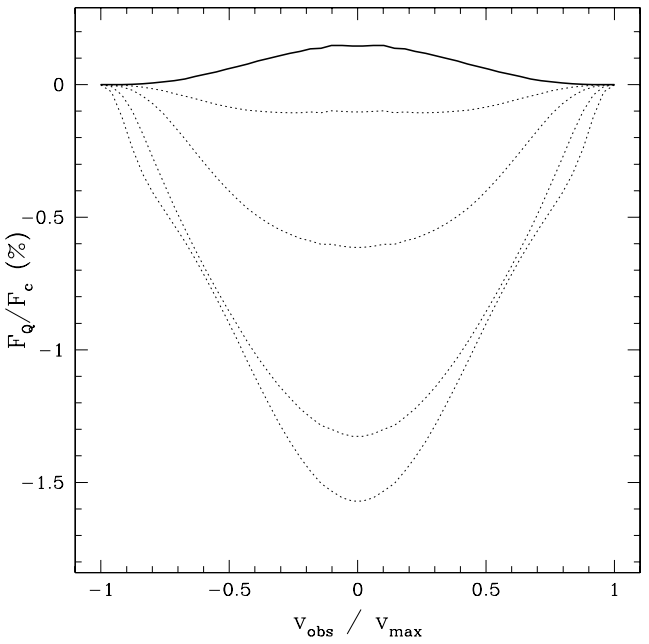

FIG. 12.—Hanle effect for a WCFields model with $v_{rot}/v_\infty = 0.08$ but with an aspherical wind. The solid line shows the line polarization that results when there is no magnetic field. The dotted lines are with the Hanle effect (to be compared with Fig. 9, *middle*). The view is edge-on, and $\tau_l = 1$ for all of the profiles. For $B = 0$, peak polarization occurs near line center and is positive because there are relatively more line scatterers in the vicinity of the equator than near the poles.

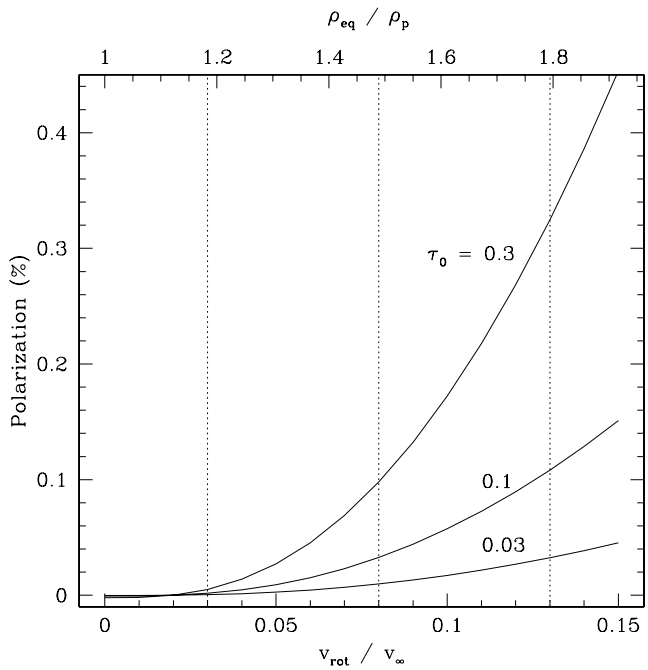

FIG. 13.—Continuum polarizations arising from Thomson scattering of starlight in the mildly distorted WCZ models. The abscissa is v_{rot}/v_∞, relevant for the models presented in this paper. Also shown at top is the corresponding asymptotic equator-to-pole density contrast. The electron scattering is assumed to be optically thin, with envelope optical depths τ_0 as indicated. These τ_0 values are for an equivalent spherical envelope. The continuum polarizations are for an edge-on view and will scale as $\sin^2 i$ for other viewing inclinations. The vertical dotted lines indicate the corresponding models used in the line calculations for the WCFields magnetic geometry assuming a spherical wind density.

because at low optical depth, most of the optically thin line radiation comes from the inner wind, where the field is largely radial with almost no Hanle effect.

Figure 11 also displays the effect of viewing inclination in the lower four panels, with the two left panels showing polarized flux in Q and U and the two right panels showing the total degree of polarization P and the polarization position angle θ_P. In each panel the line type corresponds to the same inclination angle value as indicated in the panel for F_Q.

4.2. *WCFields with an Axisymmetric Wind Density*

A net resonance line scattering polarization occurs even when there is no Hanle effect (i.e., $B = 0$), if the distribution of scatterers is asymmetric. The scattering is similar to Thomson scattering, as previously noted, reduced by the factor E_1 but increased by the much larger cross section compared to Thomson scattering.

Section 4.1 ignored this polarization contribution by assuming the wind density to be spherical. The motivation was to isolate the influence of the Hanle effect. Now relaxing this approximation, Figure 12 shows polarized line profile shapes for the case $v_{rot}/v_\infty = 0.08$ and $\gamma = 1$, which has an equator-to-pole density contrast of 1.25. The upper dark line shows the polarization from pure resonance scattering with no Hanle effect. The dotted curves show the profiles with the Hanle effect, to be compared with Figure 9, which assumed an underlying spherical wind density. Therefore, the density distribution does introduce a kind of bias for the line polarization for its interpretation in terms of the Hanle effect. However, it is not a large effect, and a strategy that targets lines with different Hanle fields should be able to correct for the influence of nonspherical density.

Allowing for $\rho(r, \mu)$ also implies that scattering polarization by free electrons in the wind may complicate the interpretation of the line polarizations. Figure 13 shows the expected continuum polarization from mildly distorted stellar winds as viewed edge-on. For this figure we are using a sequence of wind-compressed zone (WCZ) models (Ignace et al. 1996) in conjunction with the expressions of Brown & McLean (1977) for the polarization from optically thin axisymmetric envelopes. The results also include the finite star depolarization factor (Cassinelli et al. 1987). The lower axis is the ratio v_{rot}/v_∞, and the upper axis is the asymptotic value of the equator-to-pole density contrast. Electron scattering depths of $\tau_0 = 0.03$, 0.1, and 0.3 for an equivalent spherical wind were used as reference models. The three vertical dotted lines indicate the rotation values used for the Hanle effect models presented in § 4.1. Relatively few O stars are known to be intrinsically polarized at the 0.1% level, but typically $\tau_0 < 0.1$, so this is not inconsistent with the small distortions implied in our models (McDavid 2000).

In any case, continuum polarization of any kind, including interstellar polarization, is not a significant complication for our analysis: it turns out that for the strong Li-like doublets commonly observed in the UV and far-UV band, the red component has $E_1 = 0$, meaning that the line scatters isotropically, making no contribution to the line polarization and thus not being susceptible to the Hanle effect. Any polarized flux observed in the red line of the doublet must therefore arise from continuum processes, and since the doublet components are close together in frequency, the polarization of the blue component, which can show a Hanle effect, can be straightforwardly corrected for the continuum polarization.

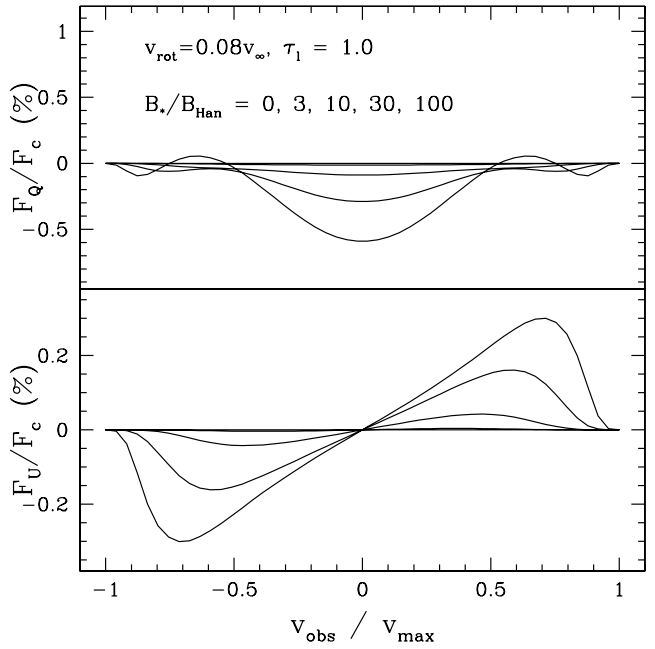

FIG. 14.—Polarized line profiles in Q and U for a WCFields model, with $v_{\rm rot}/v_\infty = 0.08$ and a spherical density, but with an initial magnetic field at the wind base that is a magnetic monopole. Compared to the basal split monopole configuration used in Fig. 9, the Q-polarization has dropped, and a significant and antisymmetric U-profile is now evident. Consequently, the U-profile, when the polarization measurement axis is aligned with the source symmetry axis, is sensitive to the symmetry of the circumstellar magnetic geometry.

4.3. *Field Topology*

The Hanle effect is sensitive to both the field strength and the magnetic geometry. This sensitivity can be made especially graphic. We previously noted that for the WCFields models, there is a small U-polarization. In Figure 14 we plot the polarized profiles for a model with $v_{\rm rot}/v_\infty = 0.08$, $i = 90^\circ$, and a spherical wind, but for a magnetic field that is initially outward radially at the wind base (i.e., a magnetic monopole: unphysical, but used here only to make a point). The result is that the Q-profiles are much reduced in scale, and a fairly substantial antisymmetric U-profile results. The models are identical in all respects to the corresponding models of Figure 9, except that the radial field in the lower hemisphere is outwardly directed instead of inwardly directed. Thus, we find that it is still the case that larger Hanle ratios yield stronger line polarizations and, moreover, that the U-profile is sensitive to the overall symmetry (top-bottom and left-right) of the global magnetic geometry.

In practice, the symmetry axis of the magnetic field (if one exists) is not known a priori. The Stokes Q and U line profiles for a source are measured according to observer-defined axes. It may be possible to identify symmetry in the magnetic field by rotating the observed polarizations using Mueller matrices to look for symmetry in the polarized profiles. Generally, a constraint on the symmetry of the circumstellar magnetic field would be estimated as part of the profile modeling.

5. DISCUSSION

This contribution has focused on the Hanle effect in resonance scattering lines common to hot star winds. We have stressed the fact that the Hanle effect is nonlinear, in that it is the nonradial field components that give rise to a change in the line polarization, yet at the same time, it is the total field strength (including the radial component) that governs the amount of the change. Consequently, the Hanle effect can be used to infer the full three-dimensional magnetic geometry in the wind. For a given set of scattering lines, stronger fields will lead to higher line polarizations. Field topology also has an influence, as evidenced by the double-peaked polarized profiles for a dipole magnetic field versus the single-peaked profiles for slow magnetic rotators.

The Far Ultraviolet Spectropolarimeter (FUSP) is a sounding-rocket payload with the goal of making the first spectropolarimetric measurements in the wavelength range of 1050–1500 Å for several stellar targets (Nordsieck et al. 2003). With a 50 cm primary, the instrument will have a spectral resolution of 0.65 Å, corresponding to a resolving power of $\lambda/\Delta\lambda = 1800$ at a wavelength of 1170 Å. This in turn corresponds to a velocity resolution of about 170 km s^{-1}, which is sufficient to resolve wind-broadened lines with typical full widths of a few thousand kilometers per second. Targeting the star ζ Ori, which was observed in the far-UV with *Copernicus* (Snow & Morton 1976), it is anticipated that FUSP will produce the first detection of the Hanle effect in a star other than the Sun.

To correctly interpret the polarization of scattering lines that will be measurable with FUSP, care must be taken to identify all sources of polarized radiation. For example, interstellar polarization is endemic to all polarimetric studies of distant objects, and there are standard techniques for its correction, based on wavelength dependence and lack of variability.

Extracting the influence of a nonspherical wind geometry on the line scattering polarization can be approached in two different ways: (1) If the interstellar polarization can be determined, the polarization outside line frequencies due to Thomson scattering can be used to model the underlying wind geometry. However, this is difficult in part because it may not be clear that the line forms in the same region that gives rise to the electron scattering polarization. (2) Alternatively, since $\boldsymbol{B}(\boldsymbol{r})$ is fixed for any given star, one can use a multiline approach to infer the polarization arising from an aspherical distribution of scatterers. Different lines have different Hanle field values, so that lines with large Hanle values can be used to estimate the nonmagnetic contribution. Once again, care must be taken, since different lines may not form in the same spatial locations; however, the P Cygni profiles themselves could be modeled to obtain information about the ionization distribution in radius and latitude.

The study of the Hanle effect for circumstellar environs and the development of radiative transport techniques is ongoing, especially in terms of relaxing the single-scattering approximation for the line polarization. In this regard one can use the expressions in Jeffery (1990) for "Sobolev-P" theory to show that the single-scattering approximation captures the flavor of the polarimetric behavior of scattering lines and that, in fact, there is nonzero polarization from line scattering even at rather high Sobolev optical depths of a few. Even at optical depths of just a few tenths, the line polarization is not truly described by single scattering. We anticipate using Monte Carlo radiation transport techniques in the future to model the line polarization more accurately. The proven versatility of these techniques will be useful in handling more realistic wind models.

Another effect ignored here needs to be explored. While our analysis applies directly to resonance transitions in ions with no nuclear spin (e.g., O VI, Si IV, C IV, Mg II, and Ca II), in other Li-like ions, such as P V, N V, Na I and K I, the presence of nuclear spin breaks the degeneracy of the spin states, and this alters the value of the polarizability E_1, making it sensitive to optical pumping. In fact, in the presence of optical pumping,

the magnetic field has another effect on the line polarization through "magnetic realignment" (Nordsieck 2001) or, in solar physics parlance, the "second Hanle effect." We are investigating the regime in which the Hanle effect and the magnetic realignment physics both apply.

We thank Jon Bjorkman for useful discussions regarding line polarization effects. We are especially grateful to the referee, Marianne Faurobert-Scholl, for several helpful comments. Support for this research comes from a grant from the National Science Foundation (AST 00-98597).

APPENDIX A

DETERMINATION OF ANGULAR QUANTITIES

The Hanle effect is complicated by the fact that three coordinate systems are involved: star, observer, and the local magnetic field orientation. A standard approach for solving for the requisite angles is to employ spherical trigonometry. More challenging are the interior angles of the spherical triangles, in part because of quadrant ambiguity and in part because of potential division-by-zero problems. An equivalent and more straightforward approach is to employ vector relations, which we describe here.

The known parameters include the stellar and observer axes and the magnetic field geometry. These immediately provide the scattering direction and vector magnetic field at any point. The stellar axes also allow one to specify the direction of the incident radiation throughout the scattering medium.

For the various spherical triangles of Fig. 3, the "arc relations" are given by dot products, with

$$\cos \vartheta_s = \hat{\boldsymbol{z}} \cdot \hat{\boldsymbol{z}}_*, \tag{A1}$$

$$\cos \vartheta_i = \hat{\boldsymbol{r}} \cdot \hat{\boldsymbol{z}}_*, \tag{A2}$$

$$\cos \chi = \hat{\boldsymbol{r}} \cdot \hat{\boldsymbol{z}}, \tag{A3}$$

$$\cos \vartheta_B = \hat{\boldsymbol{z}}_* \cdot \hat{\boldsymbol{B}}, \tag{A4}$$

$$\cos \theta_s = \hat{\boldsymbol{r}} \cdot \hat{\boldsymbol{B}}, \tag{A5}$$

$$\cos \theta_i = \hat{\boldsymbol{z}} \cdot \hat{\boldsymbol{B}}, \tag{A6}$$

where $\hat{\boldsymbol{z}} = \hat{\boldsymbol{s}}$.

Consider the spherical triangle of Fig. 15, drawn from unit vectors $\hat{\boldsymbol{a}}$, $\hat{\boldsymbol{b}}$, and $\hat{\boldsymbol{c}}$. Let the interior angles be α, β, and γ, respectively. Moreover, let the arcs be specified by θ_{ac}, θ_{ab}, and θ_{bc}. Then one can determine the cosine and sine of an interior angle by deriving the unit tangent vectors at the vertices of interest.

For example, to determine the angle α, one defines the unit tangent vectors $\hat{\boldsymbol{t}}_{ab}$ and $\hat{\boldsymbol{t}}_{ac}$ at the vertex of $\hat{\boldsymbol{a}}$ in the directions of $\hat{\boldsymbol{b}}$ and $\hat{\boldsymbol{c}}$. Then one has that

$$\cos \alpha = \hat{\boldsymbol{t}}_{ab} \cdot \hat{\boldsymbol{t}}_{ac}, \tag{A7}$$

$$\sin \alpha = \hat{\boldsymbol{a}} \cdot (\hat{\boldsymbol{t}}_{ac} \times \hat{\boldsymbol{t}}_{ab}), \tag{A8}$$

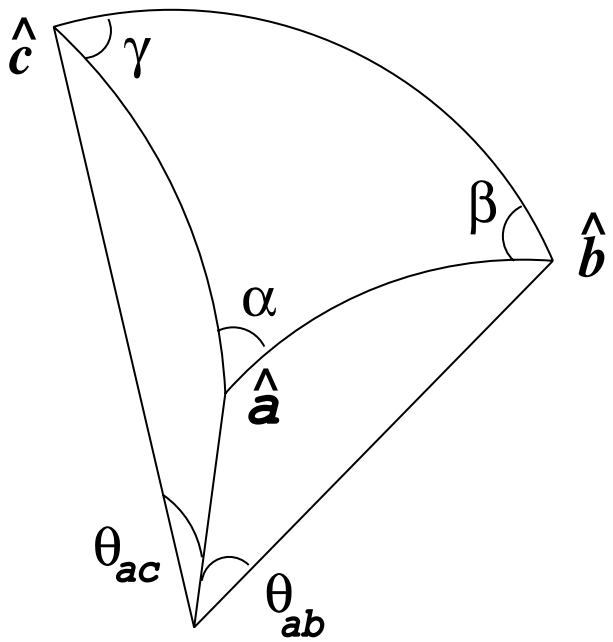

FIG. 15.—Specification of spherical triangle unit vectors, spherical polar angles, and interior angles used in relating the evaluation of the angles by vector product relations.

where the unit vectors are given by

$$\hat{\boldsymbol{t}}_{ab} = \frac{1}{\sin\theta_{ab}}\left[\left(\hat{\boldsymbol{a}}\times\hat{\boldsymbol{b}}\right)\times\hat{\boldsymbol{a}}\right], \tag{A9}$$

$$\hat{\boldsymbol{t}}_{ac} = \frac{1}{\sin\theta_{ac}}\left[\hat{\boldsymbol{a}}\times\left(\hat{\boldsymbol{c}}\times\hat{\boldsymbol{a}}\right)\right]. \tag{A10}$$

For the Hanle effect with incident unpolarized radiation, the two interior angles of relevance are i_s and δ. For the first of these, and working through the vector relations, one obtains

$$\cos i_s = (\sin\theta_s \sin\vartheta_s)^{-1}\left[\hat{\boldsymbol{B}}\cdot\hat{\boldsymbol{z}}_* - \left(\hat{\boldsymbol{z}}\cdot\hat{\boldsymbol{z}}_*\right)\left(\hat{B}\cdot\hat{\boldsymbol{z}}\right)\right], \tag{A11}$$

$$\sin i_s = (\sin\theta_s \sin\vartheta_s)^{-1}\left[\hat{\boldsymbol{z}}\cdot\left(\hat{\boldsymbol{B}}\times\hat{\boldsymbol{z}}_*\right)\right]. \tag{A12}$$

and for the second angle, one has

$$\cos\delta = (\sin\theta_s \sin\theta_i)^{-1}\left[\hat{\boldsymbol{r}}\cdot\hat{\boldsymbol{z}} - \left(\hat{\boldsymbol{z}}\cdot\hat{\boldsymbol{B}}\right)\left(\hat{\boldsymbol{B}}\cdot\hat{\boldsymbol{r}}\right)\right], \tag{A13}$$

$$\sin\delta = -(\sin\theta_s \sin\theta_i)^{-1}\left[\hat{\boldsymbol{B}}\cdot\left(\hat{\boldsymbol{z}}\times\hat{\boldsymbol{r}}\right)\right]. \tag{A14}$$

APPENDIX B

WCFIELDS FOR SLOW ROTATORS

In wind-compression theory (Bjorkman & Cassinelli 1993; Ignace et al. 1996), the distortion of the wind flow is described kinematically. Ignoring pressure gradient terms and assuming only radial forces, one can derive an expression for streamline flow. The general properties of wind compression have been confirmed with hydrodynamic simulations by Owocki et al. (1994), although the effects appear to be inhibited when nonradial accelerations that arise in the line-driving of hot star winds are included (Owocki et al. 1996).

However, retaining the basic elements of wind-compression theory, Ignace et al. (1998) extended the method to allow for "weak" magnetic fields. The key assumptions are that the magnetic field is frozen in and dominated by the hydrodynamic flow. Consequently, the known flow geometry determines the magnetic field topology.

Referring to Ignace et al. (1998) for the derivation, the key expression that determines the vector magnetic field throughout the flow is

$$\boldsymbol{B} = B_*\left(\frac{R_*^2}{r^2}\right)\left(\frac{d\mu}{d\mu_0}\right)^{-1}\frac{\boldsymbol{V}}{v_r}, \tag{B1}$$

where B_* is the surface field strength, $d\mu/d\mu_0$ is the "compression factor" that describes how neighboring streamlines evolve throughout the wind flow, $\boldsymbol{V}$ is the vector velocity in the corotating frame, and v_r is the radial velocity. All of the velocity components and the compression factor are known. The scalar strength of the field is

$$B = B_*\left(\frac{R_*^2}{r^2}\right)\left(\frac{d\mu}{d\mu_0}\right)^{-1}\left\{1+\frac{v_{\rm rot}^2}{v_r^2}\left[\frac{\sin^2\vartheta_0\cos^2\vartheta_0\sin^2\phi'}{\sin^2\vartheta}+\left(\frac{R_*}{r}\sin\vartheta_0-\frac{r}{R_*}\sin\vartheta\right)^2\right]\right\}^{1/2}, \tag{B2}$$

where $v_{\rm rot}$ is the equatorial rotation speed of the star and ϕ' is a "deflection" angle that determines the streamline flow and is described in Bjorkman & Cassinelli (1993). The zero subscript indicates a value at the base of the wind. In the upper hemisphere, streamlines move toward the equator, with $\vartheta > \vartheta_0$ for $r > R_*$. In the lower hemisphere, streamlines also move toward the equator, but with $\vartheta < \vartheta_0$. The field is taken to be radial at the wind base (split monopole) but tends to a toroidal configuration at large radius, with $B \propto r^{-1}\sin\vartheta$, like a magnetic field that is dragged out in the solar wind.

The vector orientation of the magnetic field at any point is given by the angles ϑ_B and φ_B, defined by the relations

$$\cos\vartheta_B = \hat{\boldsymbol{z}}_*\cdot\hat{\boldsymbol{B}} = \frac{B_r}{B}\cos\vartheta - \frac{B_\vartheta}{B}\sin\vartheta, \tag{B3}$$

$$\tan\varphi_B = \frac{B_{y_*}}{B_{x_*}} = \frac{B_r\sin\vartheta\sin\varphi + B_\varphi\cos\varphi + B_\vartheta\cos\vartheta\sin\varphi}{B_r\sin\vartheta\cos\varphi - B_\varphi\sin\varphi + B_\vartheta\cos\vartheta\cos\varphi}. \tag{B4}$$

Thus far, these expressions are valid for all rotation speeds for which the streamlines are not equator-crossing. The assumption of slow rotation with only mild distortions of the wind flow from spherical implies the following simplifications (Ignace 1996; J. E. Bjorkman & R. Ignace 2004, in preparation): First, the terminal speed depends only weakly on the initial latitude of a

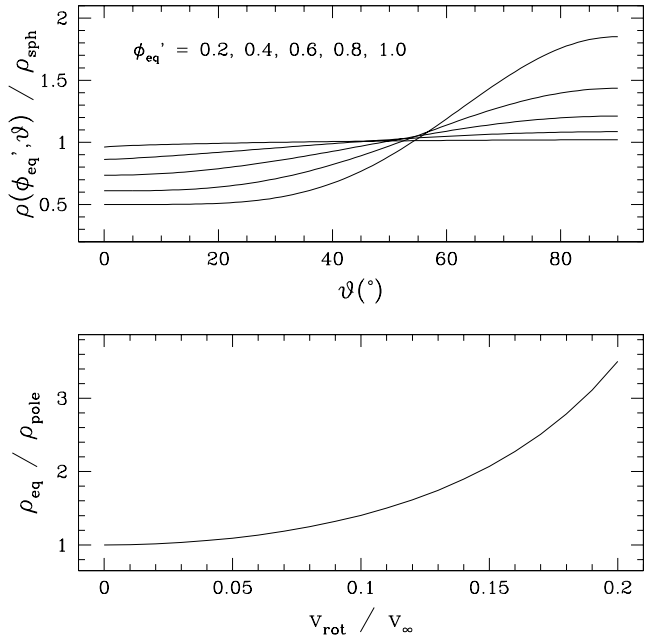

FIG. 16.—Wind geometry of WCZ models using our approximations for slowly rotating stars. *Top*: Variation of the normalized wind with density latitude ϑ at different values of ϕ'_{eq}. *Bottom*: Asymptotic wind density contrast between the equator and the pole as a function of the stellar rotation normalized to the wind terminal speed.

streamline and can thus be assumed a constant. Second, the streamline parameter becomes $\phi' \approx \phi'_{eq}(r) \sin\theta_0$, a separable function of radius and initial stellar colatitude, with

$$\phi'_{eq}(r) = \frac{v_{rot}}{\gamma v_0}\left(\frac{v_0}{v_\infty - v_0}\right)^{1/\gamma} B_Y\left(\frac{1}{\gamma},\ 1 - \frac{1}{\gamma}\right), \tag{B5}$$

where B_Y is the incomplete beta function, with $Y = 1 - v_0/v_r$. Third, the radial and latitudinal dependence of the compression factor can be fitted with the form

$$\left(\frac{d\mu}{d\mu_0}\right)^{-1} \approx \left(1 + \phi'^2_{eq}\right)^{-1} + \left[\left(\cos\phi'_{eq}\right)^{-1} - \left(1 + \phi'^2_{eq}\right)^{-1}\right] \sin^q\vartheta, \tag{B6}$$

where the exponent factor q is

$$q(r) = 3 \tan\phi'_{eq}(r). \tag{B7}$$

Consequently, the wind density as a function of radius and latitude is described by

$$\rho(r,\ \mu) = \rho_{sph}\left(\frac{d\mu}{d\mu_0}\right)^{-1}, \tag{B8}$$

where $\rho_{sph} = \rho_0 x^{-2} w^{-1}$. Figure 16 (*top*) shows the variation of the wind density with colatitude ϑ at different values of ϕ'_{eq}. Figure 16 (*bottom*) displays the asymptotic equator-to-pole density contrast ρ_{eq}/ρ_{pole} as a function of the ratio v_{rot}/v_∞.

Finally, with regard to the magnetic field, it is adequate to assume that $\vartheta_0 \approx \vartheta$, which yields for the total field strength

$$B = B_*\left(\frac{R_*^2}{r^2}\right)\left(\frac{d\mu}{d\mu_0}\right)^{-1}\left\{1 + \frac{v_{rot}^2}{v_r^2}\left[\cos^2\vartheta \sin^2\phi' + \sin^2\vartheta\left(\frac{R_*}{r} - \frac{r}{R_*}\right)^2\right]\right\}^{1/2}. \tag{B9}$$

In the special case that $\gamma = 1$, the function $\phi'_{eq}(r)$ takes on an especially simple form, with

$$\phi'_{eq}(r) = \frac{v_{rot}}{v_\infty} \ln\left(\frac{v_r}{v_0}\right). \tag{B10}$$

Since $\gamma = 1$ is the wind velocity used throughout our model line profile calculations, equation (B10) used in conjunction with the preceding expressions defines the flow geometry and the magnetic field throughout the wind.

REFERENCES

Babel, J., & Montmerle, T. 1997a, A&A, 323, 121
———. 1997b, ApJ, 485, L29
Belcher, J. W., & MacGregor, K. B. 1976, ApJ, 210, 498
Bjorkman, J. E., & Cassinelli, J. P. 1993, ApJ, 409, 429
Brown, J. C., & McLean, I. S. 1977, A&A, 57, 141
Cassinelli, J. P., Brown, J. C., Maheswaran, M., Miller, N. A., & Telfer, D. C. 2002, ApJ, 578, 951
Cassinelli, J. P., Nordsieck, K. H., & Ignace, R. 2001, in ASP Conf. Ser. 248, Magnetic Fields Across the Hertzsprung-Russell Diagram, ed. G. Mathys, S. Solanki, & D. Wickramasinghe (San Francisco: ASP), 409
Cassinelli, J. P., Nordsieck, K. H., & Murison, M. A. 1987, ApJ, 317, 290
Castor, J. I. 1970, MNRAS, 149, 111
Chandrasekhar, S. 1960, Radiative Transfer (New York: Dover)
Donati, J.-F., Babel, J., Harries, T. J., Howarth, I. D., Petit, P., & Semel, M. 2002, MNRAS, 333, 55
Donati, J.-F., Wade, G. A., Babel, J., Henrichs, H. F., de Jong, J. A., & Harries, T. J. 2001, MNRAS, 326, 1265
Drew, J. 1989, ApJS, 71, 267
Hamilton, D. R. 1947, ApJ, 106, 457
Hanle, W. 1924, Z. Phys., 30, 93
Henrichs, H. F. 2003, in ASP Conf. Ser. 305, Magnetic Fields in O, B and A Stars: Origin and Connection to Pulsation, Rotation and Mass Loss, ed. L. A. Balona, H. B. Henrichs, & R. Medupe (San Francisco: ASP), 301
Ignace, R. 1996, Ph.D. thesis, Univ. Wisconsin
———. 2001, ApJ, 547, 393 (Paper III)
Ignace, R., Cassinelli, J. P., & Bjorkman, J. E. 1996, ApJ, 459, 671
———. 1998, ApJ, 505, 910
Ignace, R., Cassinelli, J. P., & Nordsieck, K. H. 1999, ApJ, 520, 335 (Paper II)
Ignace, R., & Gayley, K. G. 2003, MNRAS, 341, 179
Ignace, R., Nordsieck, K. H., & Cassinelli, J. P. 1997, ApJ, 486, 550 (Paper I)
Jeffery, D. J. 1990, ApJ, 352, 267
Lin, H., Penn, M. J., & Kuhn, J. R. 1998, ApJ, 493, 978
Maheswaran, M., & Cassinelli, J. P. 1992, ApJ, 386, 695
McDavid, D. 2000, AJ, 119, 352
Mihalas, D. 1978, Stellar Atmospheres (San Francisco: Freeman)
Mitchell, A. C. G., & Zemansky, M. W. 1934, Resonance Radiation and Excited Atoms (Cambridge: Cambridge Univ. Press)
Moruzzi, G., & Strumia, F., eds. 1991, The Hanle Effect and Level-Crossing Spectroscopy (New York: Plenum)
Neiner, C. 2002, Ph.D. thesis, Univ. Amsterdam
Nordsieck, K. H. 2001, in ASP Conf. Ser. 248, Magnetic Fields Across the Hertzsprung-Russell Diagram, ed. G. Mathys, S. Solanki, & D. Wickramasinghe (San Francisco: ASP), 607
Nordsieck, K. H., Jaehnig, K. P., Burgh, E. B., Kobulnicky, H. A., Percival, J. W., & Smith, M. P. 2003, Proc. SPIE, 4843, 170
Owocki, S. P., Cranmer, S. R., & Blondin, J. M. 1994, ApJ, 424, 887
Owocki, S. P., Cranmer, S. R., & Gayley, K. G. 1996, ApJ, 472, L115
Penny, L. R. 1996, ApJ, 463, 737
Rybicki, G. B., & Hummer, D. G. 1978, ApJ, 219, 654
———. 1983, ApJ, 274, 380
Snow, T. P., Jr., & Morton, D. C. 1976, ApJS, 32, 429
Sobolev, V. V. 1960, Moving Envelopes of Stars (Cambridge: Harvard Univ. Press)
Stenflo, J. O. 1994, Solar Magnetic Fields (Dordrecht: Kluwer)
ud-Doula, A., & Owocki, S. P. 2002, ApJ, 576, 413
Weber, D. J., & Davis, L., Jr. 1967, ApJ, 148, 217